Article

Evaluation of Thermal Insulation of Vacuum-Insulated Casing to Prevent Uncontrollable Melting of Ice and Borehole Instability in Permafrost

Xiaohui Zhou [1], Yinao Su [1,*], Yuanfang Cheng [1,*] and Qingchao Li [1,2]

[1] School of Petroleum Engineering, China University of Petroleum (East China), Qingdao 266580, China; b17020052@s.upc.edu.cn (X.Z.); liqingchao1990@163.com (Q.L.)
[2] School of Energy Science and Engineering, Henan Polytechnic University, Jiaozuo 454000, China
* Correspondence: suyinaoupc@163.com (Y.S.); yfcheng@upc.edu.cn (Y.C.)

Abstract: During oil and gas development in permafrost, hot fluids within the wellbore can cause ice melting around wellbore and a decrease in sediment strength, as well as wellbore instability. In the present work, the experimental system for evaluating the insulation effectiveness was established, and the applicability of this experimental system and methodology was verified. It was found that the difference between the experimentally obtained and actual thermal conductivity of the ordinary casings are all within 1.0 W/(m·°C). Meanwhile, the evaluation of insulation effect found that the decrease in fluid temperature, ambient temperature, and vacuum degree can improve its insulation performance. Finally, the numerical simulation was conducted on ice melting and borehole stability during the drilling operation in permafrost. The investigation results demonstrate that the use of vacuum-insulated casings significantly reduces the total heat transferred during the simulation by 86.72% compared to the ordinary casing. The utilization of vacuum-insulated casing reduces the range of ice melting around wellbore to only 16%, which occurs when using ordinary casing. The use of the vacuum-insulated casing resulted in a reduction in the final borehole enlargement rate from 52.1% to 4.2%, and wellbore instability was effectively suppressed.

Keywords: permafrost; vacuum-insulated casing; oil and gas production; thermal conductivity; wellbore stability; ice melting

1. Introduction

As we all know, fossil fuels such as oil and gas will still be the main energy sources that restrict the development of human society for a long time in the future [1,2]. However, several onshore old oil fields located in the central and eastern regions of China have experienced a severe decline in oil production in recent years [3,4]. Using Daqing Oil Field as an example, its oil production has dropped year by year from 56 million tons in the peak period (in 1996) to 30 million tons in 2022. It is predicted that its oil production will drop sharply to 8 million tons in 2060 [3,5,6]. Meanwhile, a production increase of the newly discovered oil fields in Western China failed to make up for the widespread production decline of these oil fields. In recent years, more than 70% of the demand for crude oil and 40% of the demand for natural gas in China have to rely on imports [7]. In 2023, the overseas dependence on crude oil is expected to exceed 80%. It is no exaggeration to say that China's domestic energy security has clearly been threatened. Fortunately, the efficient exploration and development of oil and gas resources in areas such as permafrost has become an effective way to alleviate this situation.

Nevertheless, a series of issues or accidents that endangers the safety of development operation is extremely prone to occur during the production of oil and gas in the permafrost environment [8–11]. Ice melting around wellbore and borehole collapse that is prone to occur during drilling operations in permafrost is a typical one [12,13]. Figure 1 presents the

schematic diagram of this process and a brief description of its mechanism. As observed in Figure 1a, the borehole and ice in permafrost around the wellbore are both stable when the permafrost has just been drilled through. This is because the permafrost in the near-wellbore around the wellbore has not yet been disturbed by the high-temperature wellbore fluid (a mixture of drilling fluid, oil, gas, etc.) [14]. As the drilling operation continues, the ice in the permafrost around the wellbore will melt due to the long-term disturbance of high-temperature fluid within the wellbore (see Figure 1b). Ice, as a type of cement for permafrost, can enhance its strength [15]. However, the melting of ice in the near-wellbore region in drilling operations naturally makes it less cementitious, allowing borehole enlargement (collapse) to occur. Moreover, the longer the drilling operation continues, the wider the range of melting ice around the wellbore [16]. Similarly, borehole collapse will also aggravate. Since the permafrost around the wellbore at different depths is disturbed differently by drilling operations, there will inevitably be differences in borehole enlargement [17–19]. Relatively speaking, the stability of the wellbore in permafrost is worse than that of the wellbore in the conventional reservoir. The reason is that the strength of permafrost weakens as the ice in its pores melts, but conventional reservoirs do not. It is obvious that borehole collapse will affect the safety of the drilling operation, as well as the difficulty and quality of subsequent cementing operations. Normally, the cycle of the drilling operation is within 3 months and will not exceed half a year at most. However, the production of oil and gas resources typically lasts for years or even decades. The disturbance of permafrost around the wellbore caused by the development of oil and gas resources for such a long time will inevitably be much more severe than that for the drilling process [20]. Sand production is a geomechanical issue that is extremely likely to occur during long-term oil and gas development in permafrost [21,22]. Figure 2 shows the schematic diagram of sand production during long-term oil and gas production in permafrost. The severe sand production can lead to production reduction of oil and gas, even the abandonment of the wellbore [23,24]. It is of great significance for the efficient development of oil and gas in permafrost to explore measures to mitigate the risk of some geomechanical issues, such as borehole collapse.
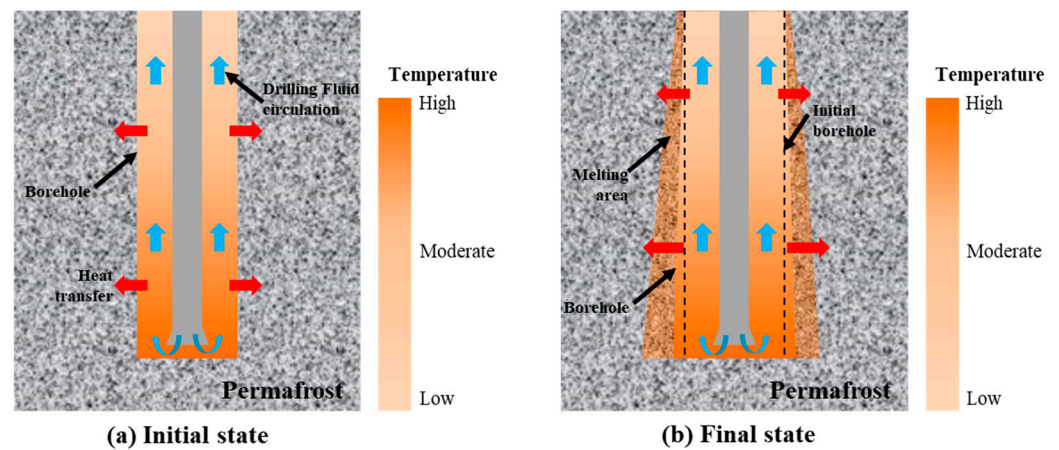

Figure 1. Schematic diagram of ice melting around wellbore and borehole collapse/enlargement during drilling operation in permafrost.
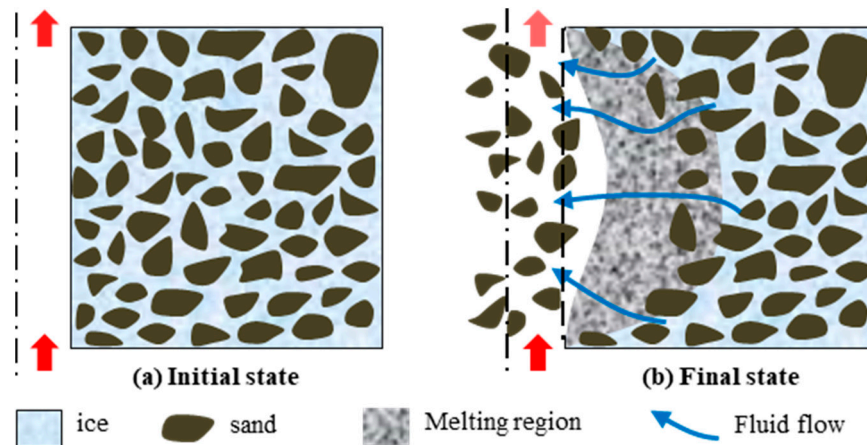
Figure 2. Schematic diagram of sand production during oil and gas production in permafrost.

To date, some investigations have been conducted to explore the effect of development operations on the stability of permafrost and wellbore. At the same time, some progress has been made. To name a few, Wang et al. (2017) numerically evaluated the impact of the thermal conductivity of cement around the wellbore on ice melting in permafrost, as well as wellhead stability [25]. According to the investigation results, it is recommended that the foam cement be used for cementing operations in permafrost to weaken the ice melting in the near wellbore. Kutasov and Eppelbaum (2017) developed a new temperature-logging processing method for determining the refreezing time of thawed formations around the wellbore in permafrost [26]. It was found that sediment refreezing time at a particular depth largely depends on the heat transferred to the formation during the drilling operation. Zhou et al. (2024) conducted a preliminary investigation on ice melting and its impact on surface and wellhead stability during oil and gas extraction in the permafrost region [27]. It was found that ice melting during the development process can cause damage to the cement–permafrost interface, leading to a wellhead sinking of up to 1.350 m. Wang et al. (2015) investigated the wellbore stability in permafrost in terms of temperature variations and time using the FLAC platform [28]. The investigation results reveal that ice content in permafrost plays a significant role in maintaining wellbore stability. All of these studies are beneficial for understanding the mechanisms of wellbore instability in permafrost.

Meanwhile, some scholars have put a lot of effort into engineering measures to weaken the disturbance of permafrost around the wellbore caused by development operations. Xie and Matthews (2011) put forward a methodology for investigating the fatal casing deformation conditions that may happen under thaw subsidence loading in permafrost [29]. It was found that the occurrence of casing failure can be avoided by following the method proposed in the study for drilling and completion design in permafrost. Wang et al. (2015) investigated the minimum wellbore pressure required to maintain wellbore stability during drilling in permafrost layers [28]. It was found that the minimum fluid pressure required for maintaining wellbore stability is a function of parameters such as pore pressure, cohesion, friction angle, and temperature difference. Based on this, the minimum drilling fluid pressure to maintain wellbore stability in permafrost before the drilling operation can be determined by engineers. Atlasov et al. (2019) proposed some engineering measures to address issues such as borehole collapse and casing failure that occur during drilling operations in permafrost [30]. These measures are conducive to the smooth implementation of drilling and completion operations in permafrost. Although these previous investigations are helpful for efficiently extracting oil and gas resources from permafrost reservoirs, there are still some shortcomings that need to be improved. Firstly, the engineering measures proposed in most previous studies are qualitative, rather than precise quantitative design or optimization [31–33]. In this way, these investigations cannot provide a substantial reference for avoiding related geomechanical issues. Secondly, there is currently a lack of investigations on avoiding some geomechanical issues from the perspective of the thermal

insulation performance of casings [34–36]. By optimizing the structure of the casing, the disturbance of thermal fluid within the wellbore to the permafrost in the near-wellbore region can be significantly weakened.

Inspired by previous investigations, the vacuum-insulated casing was designed and produced, and an experimental system for evaluating its insulation effectiveness was established. Meanwhile, the applicability of this experimental system for the evaluation of thermal insulation effectiveness was verified by comparing it with simulation results. The influence of various factors on the thermal insulation (apparent thermal conductivity) of vacuum-insulated casing was then studied. Moreover, based on this, ice melting and borehole stability in permafrost caused by the disturbance of the drilling operation was numerically investigated.

The highlights of this study can be summarized as follows:

1. A new structure of vacuum-insulated casing was designed and manufactured, and the method to determine its thermal conductivity was developed;
2. The thermal conductivity of the vacuum-insulated casing under low-temperature conditions was measured;
3. By comparison, the effect of vacuum-insulated casings on maintaining the stability of permafrost and wellbore was numerically investigated.

2. Experiments and Methods

2.1. Experimental System

To analyze the thermal insulation performance of the vacuum-insulated casing, an experimental system, as shown in Figure 3, was designed. As observed in Figure 3, the system is composed of cold storage, a fluid-heating-and-insulation system, a vacuum-insulated casing, a fluid-circulation system, and a data-measurement system. Throughout the experiment, all other parts of the experimental system should always be placed in cold storage. In the system, a combination strategy of a hard seal and a rubber gasket is used to guarantee the effective sealing of each connection point. The cold storage is used to reproduce the permafrost environment and is a rectangular space with a length, width, and height of 3 m, 4 m, and 5 m, respectively. In addition, its cooling limit is as low as −50 °C, which can reproduce the ambient temperature of almost any permafrost in the world [36]. The temperature control accuracy of the cold storage is also high enough, which is 0.05 °C. The fluid-heating-and-insulation system can provide a constant temperature circulating fluid for the entire experimental system. The fluid-heating-and-insulation system, with a heating limit of 100 °C can continuously supply circulating fluid at constant temperatures to the experimental system. The fluid-circulation system mainly consists of three parts: the high-pressure resistant tube (made of 316 L steel, inner diameter: 7 mm), the tee (thread spacing: 1 mm), and the electric diaphragm pump (lift: 30 m). To prevent heat loss in the circulation pipeline, the outside of the high-pressure pipeline is wrapped with 0.5 cm thick insulation cotton. The vacuum-insulated casing, electric heater, and pump are sequentially connected together using the high-pressure tube to form a closed system. To obtain the fluid temperature at the inlet and outlet, two thermometers are installed at the inlet and outlet of the vacuum-insulated casing through two tees, respectively. The measurement accuracy of both thermometers is 0.1 °C.

The vacuum-insulated casing is a key component of the experimental system, and it needs to be specially illustrated. The internal structures of the vacuum-insulated casing and vacuum-insulated layer are shown in Figure 4. As observed in Figure 4a,b, the main components of vacuum-insulated casing include couplings, lining pipe, outer pipe, and inner pipe. In the engineering operation, two vacuum-insulated casings were joined together via the collar and thread. In the experimental system, there is only one vacuum-insulated casing. Unfortunately, heat loss at the collar accounts for approximately 30% of the total heat loss [31]. The outer pipe is a regular 7-inch sleeve with a length of 2.0 m, and the inner pipe is a 5.5-inch casing. As observed in Figure 4c, the vacuum-insulated layer is filled with glass fibers. As is well known, glass fiber exhibits poor thermal conductivity

(about 0.04 W/(m·°C)), which can prevent a large amount of heat loss. Moreover, most of the thermal radiation inside the vacuum-insulated layer can be weakened by the aluminum foil laid between the glass fibers.
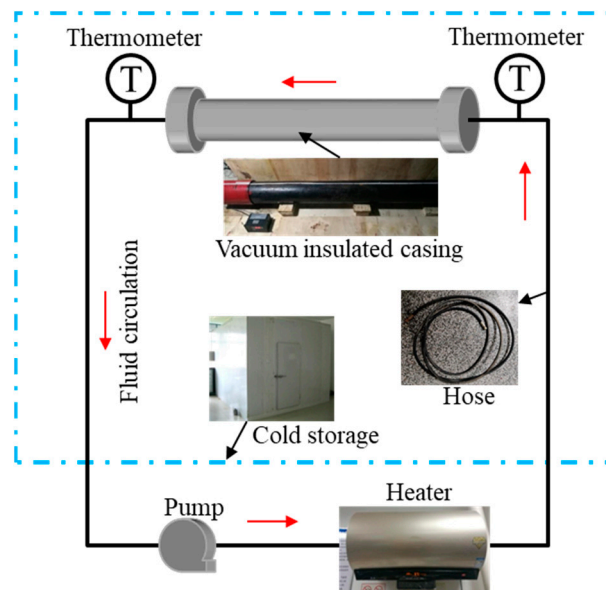

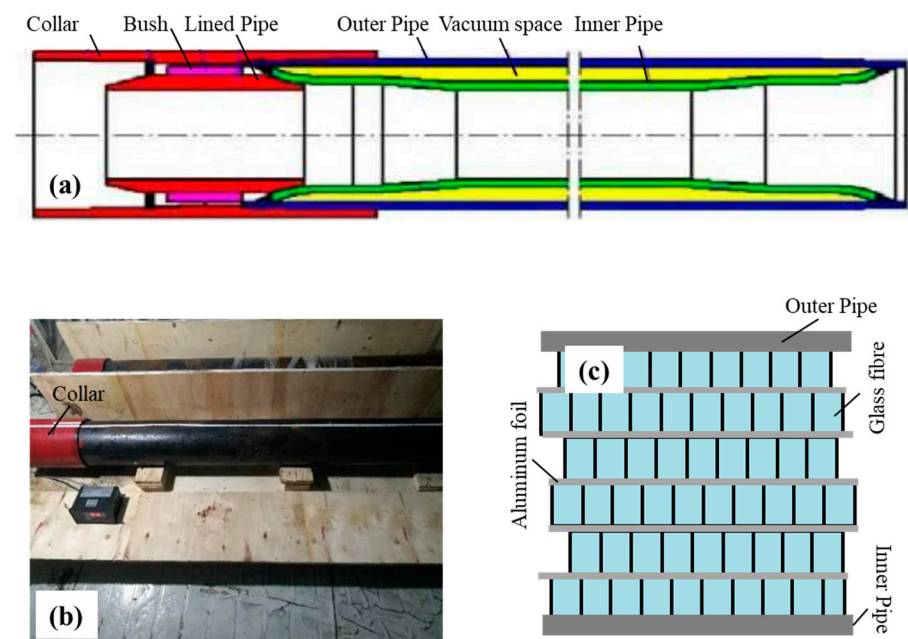**Figure 3.** Schematic diagram of the experimental system.

Figure 4. (**a**) Structure of the vacuum-insulated casing, (**b**) appearance of the vacuum-insulated casing; (**c**) layered structure of vacuum insulation layer.

2.2. Experimental Principle and Method

Throughout the experiment, the temperature of the fluid flowing inside the vacuum-insulated casing was constant, denoted as T_i. At the end of the experiment, it is necessary to measure the stable temperature of the outer wall of the vacuum-insulated casing (denoted as T_o). Then, the simulation of the heat-transfer process in the experiment was conducted with Matlab 2016 software. In simulation, the inner wall temperature of the simulation model is consistent with the fluid temperature in the experiment. In the simulation, it

is assumed that the material in the model is a single homogeneous material. When the temperature of the outer wall of the simulated model is consistent with T_o, the thermal conductivity of the simulation model is the thermal conductivity of the vacuum-insulated casing. Notably, this thermal conductivity is an apparent value. This is because the material composition of the vacuum-insulated casing is not single, its thermal conductivity should be expressed in terms of this apparent thermal conductivity. A small apparent thermal conductivity indicates better insulation performance of the casing. On the contrary, a higher apparent thermal conductivity indicates better thermal conductivity and worse thermal insulation performance of the vacuum-insulated casing.

According to the above experimental principles, the experiment in the present work can be divided into the following three steps:

1. Inspection of gas tightness of the experimental system. Firstly, the pressure inside the experimental system needs to be pumped to 1000 Pa with all valves closed. The air tightness of the experimental system is judged by observing the pressure change in the system within 48 h. If the pressure change is below 25 Pa, it indicates that the gas sealing of the experimental system is acceptable. Otherwise, the leakage point of the experimental system needs to be checked until the air tightness meets the requirements.

2. Measurement of the outer wall temperature of the casing. Firstly, the ambient temperature inside the cold storage needs to be adjusted to the pre-designed temperature. At the same time, the fluid temperature in the experimental system needs to be heated to the pre-designed temperature through the fluid-heating-and-insulation system. Subsequently, the electric diaphragm pump needs to be turned on, and the fluid will circulate in the experimental system. Finally, the outer-wall temperature of the casing can be measured when the temperature at the outlet and inlet remains unchanged for 20 min.

3. Determination of apparent thermal conductivity. Based on the experimental results, a heat-transfer simulation was conducted using Matlab 2016 software to determine the thermal conductivity of the vacuum-insulated casing.

2.3. Determination Method of Apparent Thermal Conductivity

As mentioned above, the determination of the apparent thermal conductivity is necessary for evaluating the insulation performance of the vacuum-insulated casing. Moreover, the apparent thermal conductivity is obtained through numerical simulation. To perform the heat transfer in the investigation process, the investigation model shown in Figure 5 was established. As observed in Figure 5a, the investigation model was axisymmetric, and its axis of symmetry is the wellbore axis. There are a total of 1200 elements in the model, and the size of the elements at any location is the same. The total simulation time should be slightly longer than that of the experiment corresponding to the simulation conditions. The thermal network used to describe the heat transfer occurring in the investigation process is simplified as Figure 5b. As observed in Figure 5b, the thermal resistance included in this process mainly consists of four components. R_1 and R_4 in Figure 5b represent the thermal resistance of the heat conduction process in the inner and outer pipes, respectively. Moreover, R_2 and R_3 are the thermal resistance of the heat-conduction process inside the vacuum-insulated casing and the thermal resistance of the thermal radiation process, respectively. Besides, the basis data used for determination method of apparent thermal conductivity were shown as Table 1.
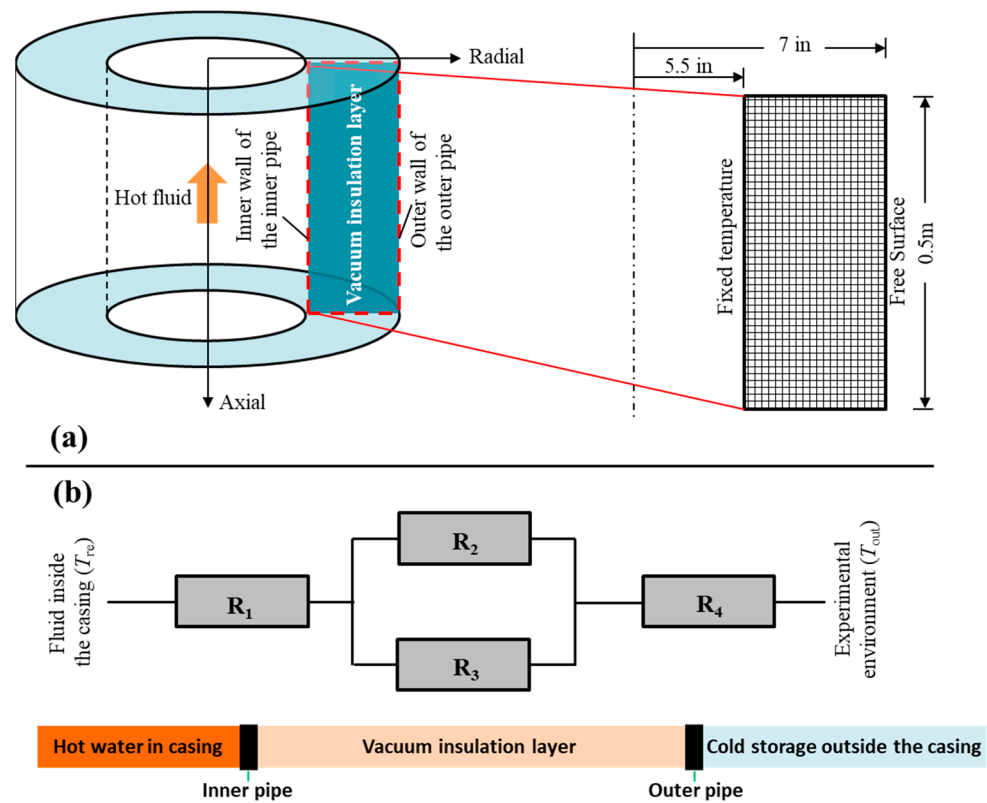
Figure 5. Schematic diagram of (**a**) model geometry for investigating the thermal insulation of the vacuum-insulated casing and (**b**) thermal network describing heat transfer occurring in the radial direction.

Table 1. Basis data used for determination method of apparent thermal conductivity.

Parameter	Unit	Value
Fluid density	kg/m^3	1000
Fluid specific heat	J/(°C·kg)	4180
Inner diameter of casing	mm	139.7
Outer diameter of casing	mm	177.8
Initial assumed thermal conductivity	W/(m·°C)	0.06
Initial vacuum degree	Pa	50
Heat-transfer coefficient	J/(m^2·s·°C)	10

The apparent thermal conductivity needs to be determined through the trial-and-error method. For the inner wall of the casing, the temperature is equal to the temperature of the fluid inside the casing. Therefore, the boundary condition of the inner wall can be expressed as

$$T_i = T_f \tag{1}$$

where T_f is the temperature of fluid in casing in °C.

If the casing is assumed to be homogeneous, the heat transfer inside the vacuum-insulated casing can be represented by the following equation [37].

$$\frac{\partial T}{\partial t} = \frac{\lambda}{c\rho}\left(\frac{\partial^2 T}{\partial x^2} + \frac{\partial^2 T}{\partial y^2}\right) \tag{2}$$

where T is the temperature in casing in °C, t is simulation time in s, λ is the thermal conductivity in W/(m·°C), c is the specific heat in J/(°C·kg), and ρ is the casing density in kg/m^3.

The convective heat transfer that occurs on the outer wall can be represented by the differential equations of heat transfer in the boundary layer, as follows [38]

$$\begin{cases} \frac{\partial u}{\partial x} + \frac{\partial v}{\partial y} = 0 \\ u\frac{\partial u}{\partial x} + v\frac{\partial v}{\partial y} = -\frac{1}{\rho}\frac{dp}{dx} - g + \frac{\mu}{\rho}\frac{\partial^2 u}{\partial y^2} \\ u\frac{\partial T}{\partial x} + v\frac{\partial T}{\partial y} = \frac{\lambda}{c\rho}\frac{\partial^2 T}{\partial y^2} \end{cases} \tag{3}$$

where u and v are the air-flow speeds in the axial (x) and radial (y) directions, respectively, in m/s, p is the air pressure in Pa, g is the gravitational acceleration, and μ is the air viscosity in mPa·s.

The stable outer-wall temperature is obtained by substituting the initial assumed thermal conductivity into the above equations. If the difference between this temperature and that obtained in experiment is less than 0.05 °C, the thermal conductivity is the apparent thermal conductivity of the vacuum-insulated casing. If not, it is necessary to readjust the thermal conductivity and repeat the simulation until the temperature-difference requirement is met.

3. Applicability Evaluation of the Investigation Methodology

Incorrect investigation methodology will inevitably lead to unreliable investigation results. Therefore, it is necessary to verify the applicability of the investigation methods before they are used to evaluate the thermal insulation of the vacuum-insulated casing. In this section, an ordinary casing (8 inches) with single composition was used to conduct verification experiments. Table 2 presents the results of validation experiments for the same casing when different experimental conditions were applied.

Table 2. Results of the validation experiments.

Fluid Temperature, °C	Cold Storage Temperature, °C	Thermal Conductivity, W/(m·°C)	
		Simulated Value	Real Value
30	−8	44.7	
30	−16	44.5	
50	−8	44.6	
50	−16	44.5	45.0
70	−8	44.4	
70	−16	44.3	

As can be seen from Table 2, the real thermal conductivity of the ordinary casing made of carbon steel is 45.0 W/(m·°C). However, the simulation results when experimental conditions are different are all slightly smaller than the real value. Nonetheless, the differences between the simulated values and real values are all less than 1.0 W/(m·°C), which is less than 2% of the real value. This is because the temperature of the inner casing wall is assumed to be constant throughout the simulation while it fluctuates due to thermal convection. Overall, the experimental values obtained based on the method proposed in this study exhibit little difference from the real values. Therefore, the investigation methodology proposed in this work is feasible for evaluating the thermal insulation of the vacuum-insulated casing.

4. Results and Discussion

Heat transfer involved in the investigation issue is mainly influenced by factors such as the material of the insulation layer of the casing. In this section, the effects of these factors on apparent thermal conductivity and the mechanisms are discussed. Finally, the synergistic effects of various factors on thermal conductivity were modeled.

4.1. Effect of Ambient Temperature

As is well known, heat transfer between the fluid and the environment outside the casing is inevitably affected by the temperature difference between the two. The effect of ambient temperature on the apparent thermal conductivity of vacuum-insulated casing is presented in Figure 6.
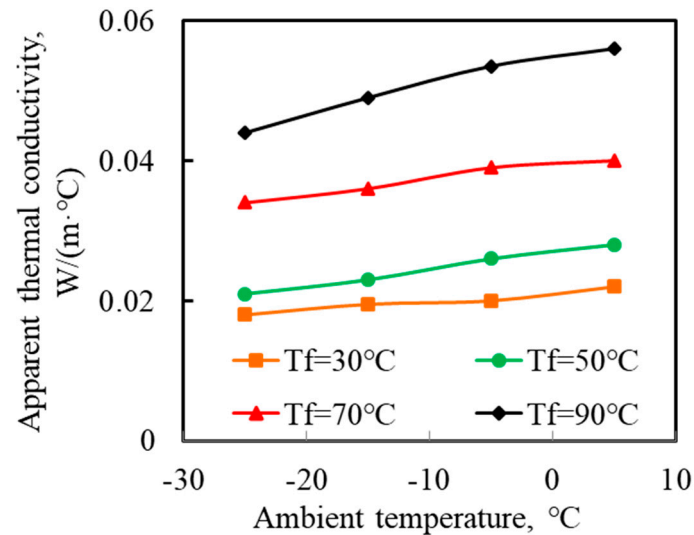

Figure 6. Effect of ambient temperature (T_a) on apparent thermal conductivity of vacuum-insulated casing.

As observed in Figure 6, the apparent thermal conductivity gradually increases with the increasing ambient temperature. Taking the fluid temperature of 90 °C as an example, the apparent thermal conductivity of the vacuum-insulated casing is only 0.044 W/(m·°C) when the ambient temperature is −25 °C. However, the apparent thermal conductivity has increased as 0.056 W/(m·°C) when the ambient temperature is 5 °C. For other fluid temperatures, the influence of the ambient temperature on the apparent thermal conductivity of the vacuum-insulated casing also shows a similar rule. This is because, for high ambient temperatures, the thermal motion and vibration of material molecules are violent, which stimulates heat transfer. Furthermore, the higher the ambient temperature, the more intense the thermal motion of molecules inside the vacuum-insulated casing will be.

Overall, the ambient temperature exhibits a significant impact on the apparent thermal conductivity of the vacuum-insulated casing. Nevertheless, the influence of ambient temperature on the apparent thermal conductivity is different in different ambient temperature ranges (see Figure 6). The apparent thermal conductivity increases rapidly as the ambient temperature increases when the ambient temperature is below −10 °C. However, once the ambient temperature is above −10 °C, the variation in apparent thermal conductivity with ambient temperature slows down. The reason is that the increase in temperature within the low-temperature range significantly stimulates the thermal vibration of the insulation material inside the insulation layer. When the temperature reaches a critical value, most molecules reach the limit in thermal vibration. In this way, the thermal motion of molecules cannot be further enhanced by increasing the temperature. Moreover, an increase in ambient temperature decreases the driving force for heat transfer, which is the temperature difference. As the ambient temperature increases, the difference between the temperature of the fluid inside the casing and the temperature of the ambient temperature outside the casing decreases. In this way, the increase in ambient temperature weakens the heat transfer to a certain extent.

To apply the experimental results to engineering optimization, mathematical modeling of the data in Figure 6 is necessary. Taking the fluid temperature of 90 °C as an example,

the relationship between the apparent thermal conductivity and ambient temperature can be described by Equation (4).

$$C_a = 0.0463e^{0.0088T_a} \tag{4}$$

where C_a is the apparent thermal conductivity, W/(m·°C). In Equation (4), the apparent thermal conductivity of the vacuum-insulated casing varies exponentially with the ambient temperature (i.e., the cold storage temperature).

4.2. Effect of Fluid Temperature

Heat transfer during the investigation process is powered by the temperature difference between the fluid (T_f) and the ambient (T_a). The fluid temperature inside the casing naturally becomes a key factor affecting the thermal conductivity of the vacuum-insulated casing.

The effect of fluid temperature on the apparent thermal conductivity of the vacuum-insulated casing is shown in Figure 7. It can be seen in Figure 7 that the apparent thermal conductivity of the vacuum-insulated casing increases significantly with the thermal fluid temperature. At an ambient temperature of −25 °C, the apparent thermal conductivity increases from 0.018 W/(m·°C) to 0.044 W/(m·°C) when the fluid temperature is raised from 30 °C to 90 °C. The reason for this is the same as for the influence of ambient temperature on thermal conductivity in the previous section. A higher fluid temperature means a higher temperature differential, which inevitably provides more adequate heat-transfer power. Due to sufficient heat-transfer power (large temperature difference) and active molecular vibration, a large amount of heat is transferred from the fluid inside the casing to its outside [39]. The vacuum-insulated casing demonstrates high thermal conductivity while exhibiting poor insulation performance at a macroscopic level. Nevertheless, the influence of fluid temperature on the thermal conductivity of the vacuum-insulated casing varies inconsistently across all fluid temperature ranges. When the fluid temperature exceeds 50 °C, the effect of the fluid temperature on the thermal conductivity is stronger than when it is below this temperature. If the ambient temperature is 5 °C, the average rate of change of thermal conductivity with the fluid temperature is 0.0003 W/(m·°C^2) when the fluid temperature is below 50 °C. However, this value has increased to 0.0007 W/(m·°C^2) when the fluid temperature is higher than 50 °C.
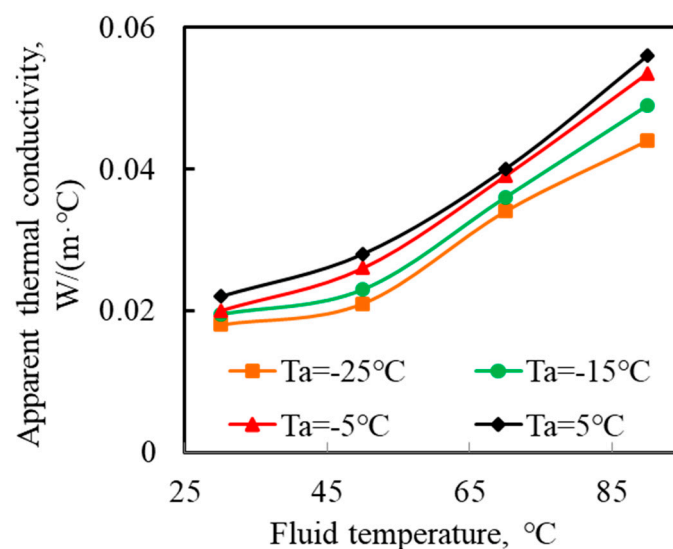

Figure 7. Effect of fluid temperature (T_f) on apparent thermal conductivity of vacuum-insulated casing.

Ambient temperature has a greater impact on thermal conductivity than fluid temperature, as demonstrated by Figures 6 and 7. The conclusion is strongly supported by the slope of each curve in the two figures. By comparison, it was found that the slopes of

the four curves in Figure 7 are significantly larger than those of the four curves in Figure 6. Meanwhile, the influence of fluid temperature on the apparent thermal conductivity exhibits significant differences across temperature ranges. Higher fluid temperatures increase the driving force for heat transfer, resulting in a stronger heat transfer and higher apparent thermal conductivity.

Similarly, the effect of fluid temperature on the apparent thermal conductivity of the vacuum-insulated casing shown in Figure 7 was also modeled. For an ambient temperature of $-25\,°C$, the relationship between the fluid temperature on apparent thermal conductivity can be expressed by the following equation.

$$C_f = 0.1724e^{-0.037T_f} \tag{5}$$

where C_f is the apparent thermal conductivity affected by fluid temperature, $W/(m·°C)$. The simulation results of ice melting and wellbore collapse in permafrost determined with the help of this fitting equation can provide reverse guidance for the design of drilling fluid and vacuum-insulated casing.

4.3. Effect of Vacuum Degree

The thermal vibration of gas molecules inside the insulation layer is also an important factor affecting heat transfer. Herein, the concept of "vacuum degree" is used to represent the pressure value inside the insulation layer that is higher than the absolute vacuum (0 Pa). A high vacuum degree within the insulation layer leads to a reduction in the number of gas molecules, resulting in improved thermal insulation. In this study, the change in vacuum degree in the insulation layer was realized using a vacuum pump with a pumping rate of 4 L/s.

Figure 8 shows the relationship between the apparent thermal conductivity and the vacuum degree when the fluid and ambient temperatures are $-20\,°C$ and $90\,°C$, respectively. From Figure 8, it can be seen that when the vacuum degree exceeds 20,000 Pa, the change in vacuum degree actually does not show a significant impact on thermal conductivity. However, when the vacuum degree is lower than 20,000 Pa, a slight change in the vacuum degree of the insulation layer can cause a significant change in the apparent thermal conductivity. When the vacuum degree of the insulation layer increased from 20,000 Pa to 80,000 Pa, the apparent thermal conductivity only increased by 0.006 $W/(m·°C)$. However, when the vacuum degree of the insulation layer decreases from 20,000 Pa to 10 Pa, the decrease in apparent thermal conductivity is as high as 0.035 $W/(m·°C)$.
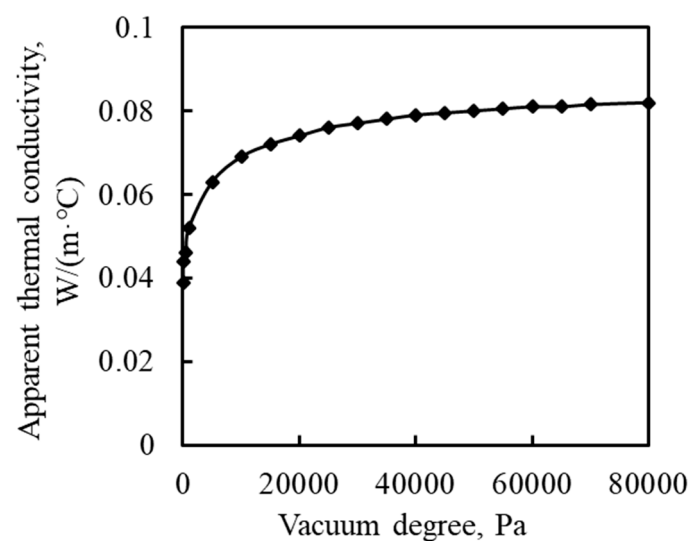

Figure 8. Effect of vacuum degree on apparent thermal conductivity of vacuum-insulated casing.

The mechanism can be revealed through the schematic diagram shown in Figure 9. As presented in Figure 9a, when the vacuum degree is low, the sparse gas molecules cannot make the thermal vibration space of all molecules occupy most of the study space. In this case, a slight change in the vacuum degree can greatly affect the proportion of the total molecular vibration space in the study space. However, when the vacuum degree is high, the total vibration space of all molecules occupies an extremely high proportion of the study space (see Figure 9b). Adding more molecules (increasing the vacuum degree) in the study space does not significantly increase this proportion, nor does it greatly excite heat transfer.
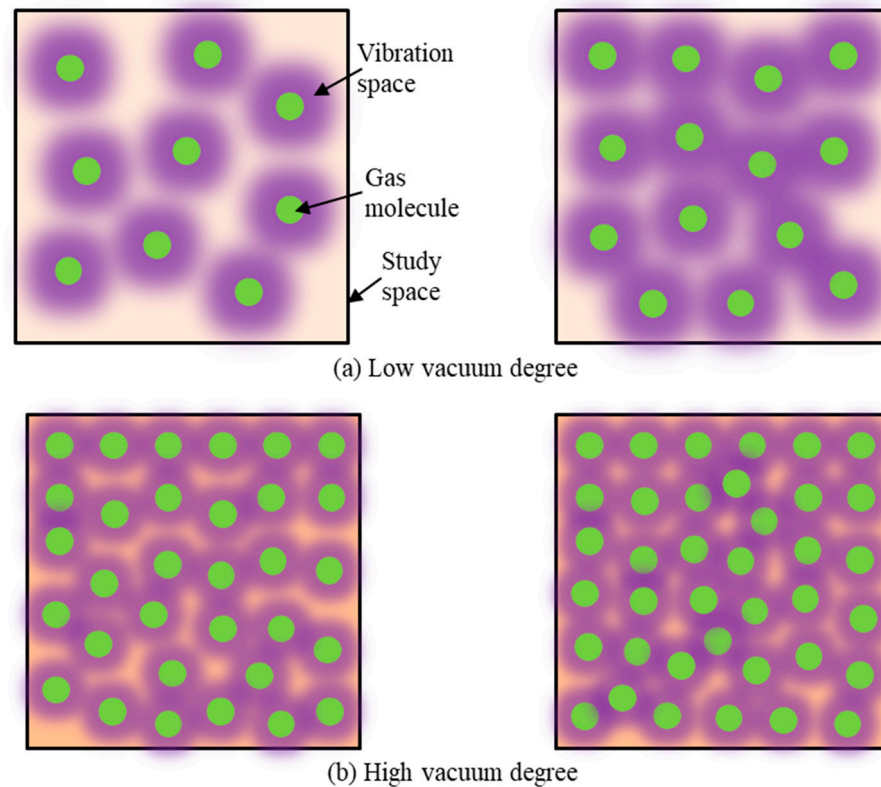

Figure 9. Schematic diagram of the mechanism of the influence of vacuum degree on the apparent thermal conductivity.

The relationship between apparent thermal conductivity and the vacuum degree of the insulation layer can be fitted as the following equation.

$$C_v = 0.0057 \ln(P_v) + 0.0171 \tag{6}$$

where C_v is the apparent thermal conductivity affected by vacuum degree, W/(m·°C).

4.4. Modeling Synergistic Effect of Multiple Factors on Thermal Conductivity

In Sections 4.1–4.3, the influence of different factors on the apparent thermal conductivity is illustrated. Unfortunately, there is a synergistic effect of these factors on the apparent thermal conductivity. Describing the synergistic impact of multiple factors on apparent thermal conductivity by one model is indeed a challenge.

To model this synergistic effect, the comprehensive coefficient as the product of C_a, C_f, and C_v parameters is defined. Notably, the comprehensive coefficient is an intermediate parameter and has no actual physical significance. The variation of the comprehensive

coefficient with apparent thermal conductivity is shown in Figure 10, and the relationship between them can be expressed as

$$\omega = C_a \cdot C_f \cdot C_v = 2 \times 10^{-4} C + 4 \times 10^{-7} \tag{7}$$

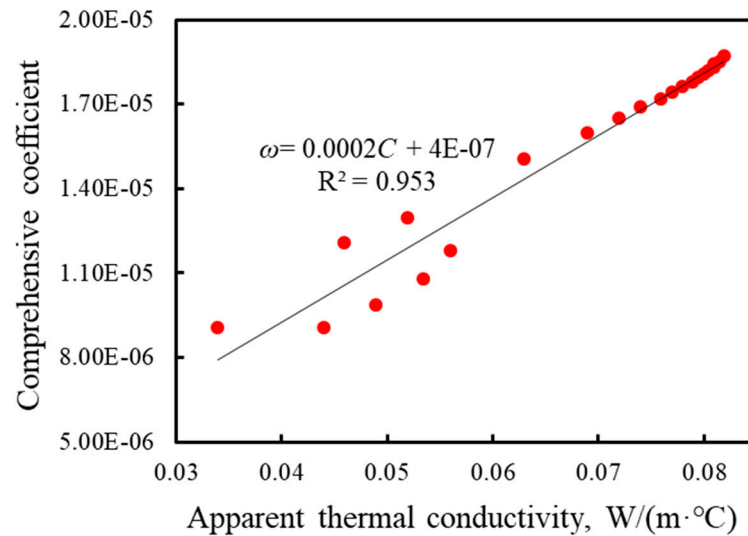where ω is the comprehensive coefficient, dimensionless.

Figure 10. Relationship between the comprehensive coefficient with apparent thermal conductivity of the vacuum-insulated casing.

The model that describes the relationship between the apparent thermal conductivity and three factors can be obtained by sorting out Equation (7), and it was expressed as follows.

$$C = 0.0112 e^{0.0493 T_a} \cdot 862 e^{-0.037 T_f} \cdot (285 \ln(P_v) + 85.5) - 0.002 \tag{8}$$

where C is the apparent thermal conductivity affected by multiple factors, W/(m·°C).

5. Role of Vacuum-Insulated Casing in Mitigating Ice Melting and Wellbore Instability

A numerical investigation was conducted to highlight the effectiveness of vacuum-insulated casing in mitigating ice melting around the wellbore and preventing wellbore instability during permafrost drilling.

5.1. Mathematical Model

The numerical analysis of wellbore stability in permafrost involves processes such as heat transfer, sediment deformation, ice melting, and water seepage. The numerical model will inevitably exhibit strong nonlinearity due to the complex coupling between various physical fields [10].

During the drilling operation, the energy-conservation equation of the permafrost around the wellbore can be expressed as [10]

$$\left[\begin{array}{c} (1 - \varphi)\rho_r C_{pr} + \varphi S_i \rho_i C_{pi} + \\ \varphi S_g \rho_g C_{pg} + \varphi S_w \rho_w C_{pw} \end{array} \right] \frac{\partial T}{\partial t} + \nabla \cdot \left[\begin{array}{c} (\rho_g u_g C_{pg} + \\ \rho_w u_w C_{pw})T \end{array} \right] - \nabla \cdot (\lambda_c \nabla T) = -m_i \Delta H_D \tag{9}$$

where λ_C is the thermal conductivity in W/(m·°C), T is the temperature in °C, ρ is the density in kg/m³, u is seepage velocity in m/s, H is enthalpy in J/kg, φ is the porosity, t is time in s, and S is the saturation of fluid in sediment. m_i is the melting rate of ice in kg/(m³·s). The subscripts r, i, g, and w are the permafrost skeleton for ice, gas, and water, respectively.

During drilling operations, the melting of ice can cause changes in the water and gas saturation within the permafrost. Then, the seepage of gas and water will occur in the permafrost around the wellbore. Taking the deformation of the permafrost skeleton into account, the seepage continuity equations of gas, water, and ice can be expressed as Equation (10) [10].

$$
\begin{cases}
\text{Gas}: \ -\nabla \cdot \left(\varphi \rho_g S_g \left(u_g + u_r\right)\right) + q_g = \frac{\partial(\varphi \rho_g S_g)}{\partial t} \\
\text{Ice}: \ -\nabla \cdot \left(\varphi \rho_i S_i u_i\right) - m_i = \frac{\partial(\varphi \rho_i S_i)}{\partial t} \\
\text{Water}: \ -\nabla \cdot \left(\varphi \rho_w S_w (u_w + u_r)\right) + m_w + q_w = \frac{\partial(\varphi \rho_w S_w)}{\partial t}
\end{cases} \tag{10}
$$

where q_g and q_w are the source and sink items of gas and water, respectively. u is the seepage velocity in m/s. m_w is production rate of water caused by ice melting in kg/(m^3·s).

The relationship between the saturation of water (S_w), gas (S_g), and ice (S_i) in permafrost pores can be expressed by Equation (11).

$$
S_g + S_i + S_w = 1 \tag{11}
$$

Meanwhile, the seepage equations of gas and water in permafrost can be expressed as [10]

$$
\begin{cases}
\text{Gas}: \ \varphi S_g \left(u_g + u_r\right) = -Kr_g K / \mu_g \left(\nabla P_g + \rho_g g\right) \\
\text{Water}: \ \varphi S_w (u_w + u_r) = -Kr_w K / \mu_w \left(\nabla P_w + \rho_w g\right)
\end{cases} \tag{12}
$$

where μ is the viscosity in cP and Kr is the relative permeability in mD.

By substituting Equation (12) into Equation (10), the seepage equation expressed in terms of gas-phase pressure (P_g) can be obtained, and it was written as [10]

$$
\begin{aligned}
-\nabla \cdot \left(\left(\frac{Kr_g K \rho_g}{\mu_g} + \frac{Kr_w K \rho_w}{\mu_w} \right) \nabla P_g \right) \ &= q_g + q_w + m_w - \left(\rho_g S_g + \rho_w S_w\right) \frac{\partial \varepsilon_v}{\partial t} \\
&\quad - \varphi \frac{\partial(\rho_g S_g + \rho_w S_w)}{\partial t} + \nabla \cdot \left(\left(\frac{Kr K \rho_g^2}{\mu_g} + \frac{Kr_w K \rho_w^2}{\mu_w} \right) g \right) \\
&\quad - \nabla \cdot \left(\frac{K_{rw} K \rho_w}{\mu_w} \nabla P_c \right)
\end{aligned} \tag{13}
$$

where ε_v is the strain of permafrost in the near-wellbore region and P_c is the capillary pressure.

The static equilibrium-differential equation of permafrost can be expressed as

$$
\begin{cases}
\frac{\partial \sigma_x}{\partial x} + \frac{\partial \tau_{xy}}{\partial y} + \frac{\partial \tau_{xz}}{\partial z} + f_x = 0 \\
\frac{\partial \sigma_y}{\partial y} + \frac{\partial \tau_{xy}}{\partial x} + \frac{\partial \tau_{yz}}{\partial z} + f_y = 0 \\
\frac{\partial \sigma_z}{\partial z} + \frac{\partial \tau_{xz}}{\partial x} + \frac{\partial \tau_{xz}}{\partial y} + f_z = 0
\end{cases} \tag{14}
$$

where σ_x, σ_y, and σ_z are the normal stress components in three directions in MPa. τ_{xy}, τ_{xz}, and τ_{yz} are the shear-stress components in MPa. f_x, f_y, and f_z are the body forces in three directions in MPa.

The deformation of permafrost can be indirectly described by the parameter of strain. Fortunately, the geometric equation characterizes the relationship between displacement and strain in finite-element analysis. The geometric equation for wellbore-stability analysis during drilling in permafrost can be expressed as

$$
\varepsilon_{ij} = \frac{1}{2} \left(u_{i,j} + u_{j,i} \right) \tag{15}
$$

In this study, the Mohr–Coulomb criterion was used to describe the stress–strain relationship of permafrost, which can be written as

$$
\begin{cases}
d\sigma = \left[[D_e] - \frac{[D_e]\left\{\frac{\partial F}{\partial \sigma}\right\}\left\{\frac{\partial F}{\partial \sigma}\right\}^T [D_e]}{A + \left\{\frac{\partial F}{\partial \sigma}\right\}^T [D_e]\left\{\frac{\partial F}{\partial \sigma}\right\}} \right] d\varepsilon \\
F = \frac{1}{2}(\sigma_1 - \sigma_3) - \frac{1}{2}(\sigma_1 + \sigma_3) \cdot \sin(\theta) - Co \cdot \cos(\theta)
\end{cases} \tag{16}
$$

where D_e is the elastic matrix, F is the yield function, and A is the hardening index. σ_1 and σ_3 are the maximum and minimum stress components, Co is the cohesion, and θ is the internal friction angle.

5.2. Mechanical Properties of Permafrost

Many previous studies have revealed that the mechanical properties of permafrost change with temperature. In other words, the mechanical properties of permafrost are temperature-dependent. In the present work, cohesion, the internal friction angle, Young's modulus, and Poisson's ratio of the permafrost at different temperatures can be determined with the following formulae [40,41].

Cohesion (*Co*):

$$Co(\text{kPa}) = \begin{cases} 20 + 6(T_0 - T)^{1.24} & T \leq T_0 \\ 20 & T > T_0 \end{cases} \tag{17}$$

internal friction angle (θ):

$$\theta(°) = \begin{cases} 20 + 3.4(T_0 - T)^{0.38} & T \leq T_0 \\ 20 & T > T_0 \end{cases} \tag{18}$$

Young's modulus (*E*)

$$E(MPa) = \begin{cases} 20 + 11.3(T_0 - T)^{0.6} & T \leq T_0 \\ 20 & T > T_0 \end{cases} \tag{19}$$

Poisson's ratio (ν)

$$\nu = \begin{cases} 0.28 - 0.007(T_0 - T) & T \leq T_0 \\ 0.28 & T > T_0 \end{cases} \tag{20}$$

In the four equations, T_0 is 0 °C.

5.3. Discretization of the Mathematical Model

The weak integral forms of each control equation included in the model are implemented using the Galerkin algorithm.

(1) Discretization of the temperature field equation

The weak integral form of the temperature field equation in the space domain is obtained by combining the temperature boundary conditions, which can be expressed as

$$[M]^e\{T\}^e + [K]^e\{T\}^e = \{f\}^e \tag{21}$$

where

$$\begin{cases} [M]^e = \int\limits_{\Omega} N^T\left[(1-\varphi)\rho_r C_{pr} + \varphi S_i \rho_i C_{pi} + \varphi S_g \rho_g C_{pg} + \varphi S_w \rho_w C_{pw}\right] N dV \\ [K]^e = \int\limits_{\Omega} \nabla N^T\left(\lambda_c \nabla N - (\rho_g u_g C_{pg} + \rho_w u_w C_{pw})N\right)dV \\ \{f\}^e = \{f_1\}^e + \{f_2\}^e + \{f_3\}^e \\ \{f_1\}^e = -\int\limits_{\Omega} N^T(m_i \Delta H_m)dV \\ \{f_2\}^e = -\int\limits_{\Omega} N^T Q_{in} dV \\ \{f_3\}^e = \int\limits_{\Gamma} N^T f_T(x,z,t)dS \end{cases}$$

The weak integral form of the temperature-field equation in the time domain can be written as

$$\left([M]^j_{n+1} + [K]^j_{n+1}\Delta t\right)\{T\}^{j+1}_{n+1} = \{f\}^j_{n+1}\Delta t + [M]^j_{n+1}\{T\}_n \tag{22}$$

where

$$
\begin{cases}
[M]^j_{n+1} = \int\limits_\Omega N^T \Big[(1-\varphi)_n (\rho_r C_{pr})^j_{n+1} + \varphi_n \big(S_i \rho_i C_{pi} + S_g \rho_g C_{pg} + S_w \rho_w C_{pw} \big)^j_{n+1} \Big] N dV \\[2mm]
[K]^j_{n+1} = \int\limits_\Omega \nabla N^T \Big((\lambda_c)^j_{n+1} \nabla N - \big(\rho_g u_g C_{pg} + \rho_w u_w C_{pw} \big)^j_{n+1} N \Big) dV \\[2mm]
\{f\}^j_{n+1} = \{f_1\}^j_{n+1} + \{f_2\}^j_{n+1} + \{f_3\}^j_{n+1} \\[2mm]
\{f_1\}^j_{n+1} = -\int\limits_\Omega N^T (m_i \Delta H_m)^j_{n+1} dV \\[2mm]
\{f_2\}^j_{n+1} = -\int\limits_\Omega N^T (Q_{in})^j_{n+1} dV \\[2mm]
\{f_3\}^j_{n+1} = \int\limits_\Gamma N^T \Big(f_T(x,z,t)^j \Big)_{n+1} dS
\end{cases}
$$

(2)   Discretization of the seepage-field equation

The weak integration form of the seepage-field equation was obtained with integration by parts on all items on the left side of it. It can be written as the following equation.

$$
[Q]^e \{P_g\}^e = \{f\}^e \tag{23}
$$

where

$$
\begin{cases}
[Q]^e = \int\limits_\Omega \nabla N^T \left(\dfrac{K_{rg} K \rho_g}{\mu_g} + \dfrac{K_{rw} K \rho_w}{\mu_w} \right) \nabla N^T dV \\[3mm]
\{f\}^e = \{f_1\}^e + \{f_2\}^e + \{f_3\}^e + \{f_4\}^e + \{f_5\}^e + \{f_6\}^e \\[2mm]
\{f_1\}^e = \int\limits_\Omega N^T (q_g + q_w + m_g + m_w) dV \\[3mm]
\{f_2\}^e = -\int\limits_\Omega N^T \left((\rho_g S_g + \rho_w S_w) \dfrac{\partial \varepsilon_v}{\partial t} \right) dV \\[3mm]
\{f_3\}^e = -\int\limits_\Omega N^T \left(\varphi \dfrac{\partial (\rho_g S_g + \rho_w S_w)}{\partial t} \right) dV \\[3mm]
\{f_4\}^e = -\int\limits_\Omega \nabla N^T \left(\left(\dfrac{K_{rg} \rho_g^2}{\mu_g} + \dfrac{K_{rw} \rho_w^2}{\mu_w} \right) K g \right) dV \\[3mm]
\{f_5\}^e = \int\limits_\Omega \nabla N^T \left(\dfrac{K_{rw} \rho_w}{\mu_w} K \nabla P_c \right) dV \\[3mm]
\{f_6\}^e = -\int\limits_\Gamma N^T (q_g + q_w) dS
\end{cases}
$$

Similar to the temperature-field equation, the seepage-field equation also needs to be discretized and decoupled in the time domain. The fully implicit decoupling form of the seepage field equation in the time domain can be written in the following form.

$$
[Q]^j_{n+1} \{P_g\}^{j+1}_{n+1} = \{f\}^j_{n+1} \tag{24}
$$

where

$$
\begin{cases}
[Q]^j_{n+1} = \int\limits_\Omega \nabla N^T \left(\dfrac{K^j_{rg}\rho^j_g}{\mu^j_g} K^j + \dfrac{K^j_{rw}\rho^j_w}{\mu^j_w} K^j \right)_{n+1} \nabla N dV \\[4mm]
\{f\}^j_{n+1} = \{f_1\}^j_{n+1} + \{f_2\}^j_{n+1} + \{f_3\}^j_{n+1} + \{f_4\}^j_{n+1} + \{f_5\}^j_{n+1} + \{f_6\}^j_{n+1} \\[2mm]
\{f_1\}^j_{n+1} = \int\limits_\Omega N^T \left(q_g{}^j + q_w{}^j + m_g{}^j + m_w{}^j \right)_{n+1} dV \\[4mm]
\{f_2\}^j_{n+1} = -\int\limits_\Omega N^T \left(\left(\rho_g{}^j S_g{}^j + \rho_w{}^j S_w{}^j \right)_{n+1} \dfrac{(\varepsilon_v)_n - (\varepsilon_v)_{n-1}}{\Delta t} \right) dV \\[4mm]
\{f_3\}^j_{n+1} = -\int\limits_\Omega N^T \left(\varphi_n \dfrac{(\rho_g S_g + \rho_w S_w)_n - (\rho_g S_g + \rho_w S_w)_{n-1}}{\Delta t} \right) dV \\[4mm]
\{f_4\}^j_{n+1} = -\int\limits_\Omega \nabla N^T \left(\left(\left(\dfrac{K_{rg}}{\mu_g} \right)^j_{n+1} \left(\rho^2_g \right)^j_{n+1} + \left(\dfrac{K_{rw}}{\mu_w} \right)^j_{n+1} \left(\rho^2_w \right)^j_{n+1} \right) [K]^j_{n+1} g \right) dV \\[4mm]
\{f_5\}^j_{n+1} = \int\limits_\Omega \nabla N^T \left(\left(\dfrac{K_{rw}}{\mu_w} [K] \right)^j_{n+1} (\rho_w)^j_{n+1} (\nabla P_c)^j_{n+1} \right) dV \\[4mm]
\{f_6\}^j_{n+1} = -\int\limits_\Gamma N^T \left(q_g{}^j + q_w{}^j \right)_{n+1} dS
\end{cases}
$$

(3)   Discretization of the stress-field equation

The decoupling expression of the stress-field equation expressed in incremental form in the space domain was acquired by substituting the constitutive equation into it, which was expressed as Equation (25).

$$
[K_T]^e \{\Delta u^e\} = [L]^e \{\Delta P^e\} + \{\Delta R^e\} \tag{25}
$$

in this equation

$$
\begin{cases}
[K_T]^e = \int\limits_\Omega B^T D_e B dV \\[3mm]
[L]^e = \int\limits_\Omega B^T m\alpha N dV \\[3mm]
\{\Delta R^e\} = \{\Delta R^t\} - \{R^t\} \\[2mm]
\{\Delta R^t\} = \int\limits_\Omega N^T \Delta F_i dV + \int\limits_\Gamma N^T \Delta T_i dS \\[3mm]
\{R^t\} = \int\limits_\Omega B^T \sigma_{ij} dV - \int\limits_\Omega B^T m\alpha P dV - \int\limits_\Omega N^T F_i dV - \int\limits_\Gamma N^T T_i dS
\end{cases}
$$

For the balance equation in the stress field, it does not need to be decoupled in the time domain. Therefore, there is no decoupling form of the balance equation of the stress field in the time domain. After obtaining the decoupling forms of the control equations for each physical field, numerical solutions can be performed. The simulation is coded with the Matlab 2016 platform, and the implementation workflow is shown in Figure 11.
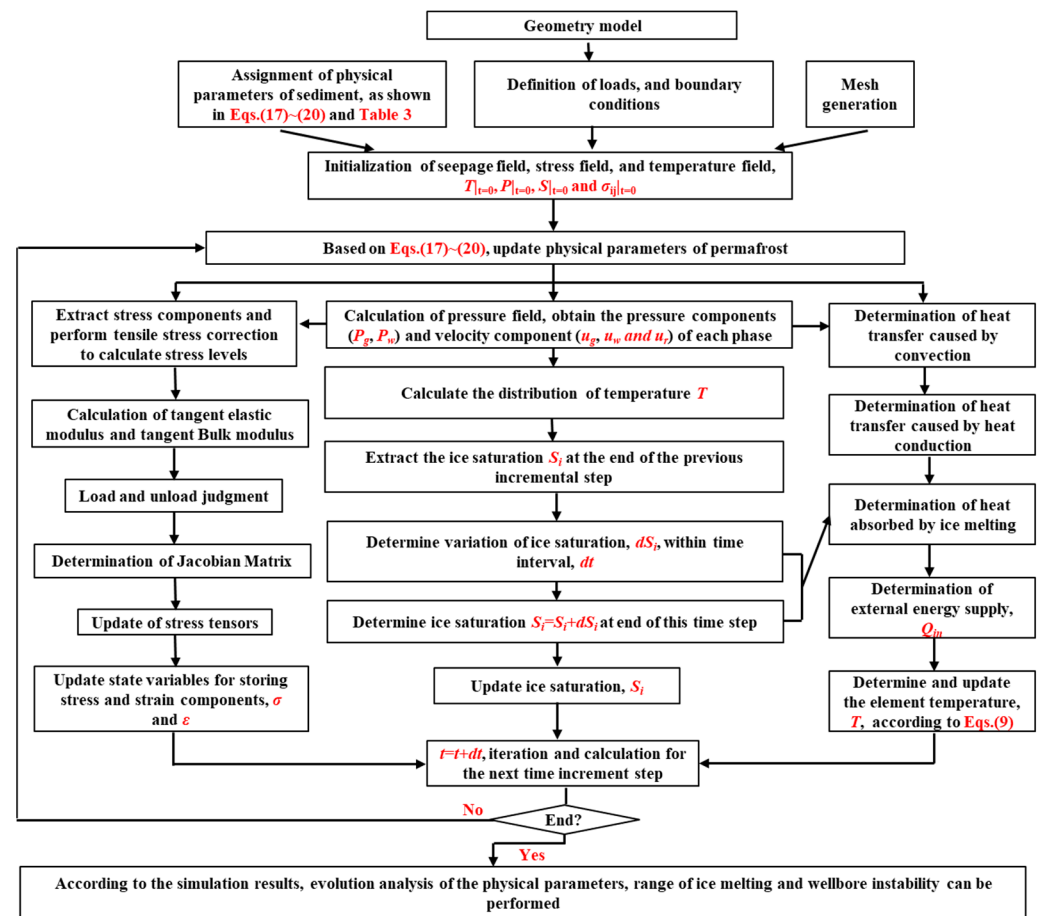
Figure 11. Workflow for numerically solving the mathematical model.

5.4. Model Geometry and Boundary Conditions

Figure 12 presents the geometry of the model used for wellbore stability in permafrost. As can be observed in Figure 12, the model consists of two parts, namely permafrost and vacuum-insulated casing. A square permafrost with a side length of 15 m is the main component of the investigation model, with the 8.5-inch (21.59 cm) wellbore at its center. Moreover, the permafrost in the model is assumed to be homogeneous. Inside the wellbore, a 7-inch vacuum-insulated casing is well-cemented on the borehole. Ice melting and wellbore instability mainly occur in the near-wellbore region; the size of elements within 5 m around the wellbore is smaller than that near the outer boundary. Furthermore, the size of the elements closer to the well wall is smaller. Moreover, the element size of the casing is consistent with the size of the adjacent permafrost elements.

On the outer boundaries (AB, BC, CD, and DA), temperature and pore pressure boundary conditions need to be assigned throughout the simulation. Of course, the values correspond to the sediment temperature and sediment pressure at the depth where the model is located, respectively. At the same time, loads with values equal to the maximum (σ_H) and minimum (σ_h) horizontal principal stresses need to be applied on the outer boundaries. Except for a load equal to the bottom-hole pressure, a temperature boundary condition equal to the drilling fluid temperature also needs to be applied to the inner wall of the casing. Additionally, the permafrost in the model also needs to be assigned the initial pore pressure, the initial ice saturation, the initial temperature, and the initial in-situ stresses. Basic data for the simulation of ice melting and wellbore stability were displayed in Table 3.
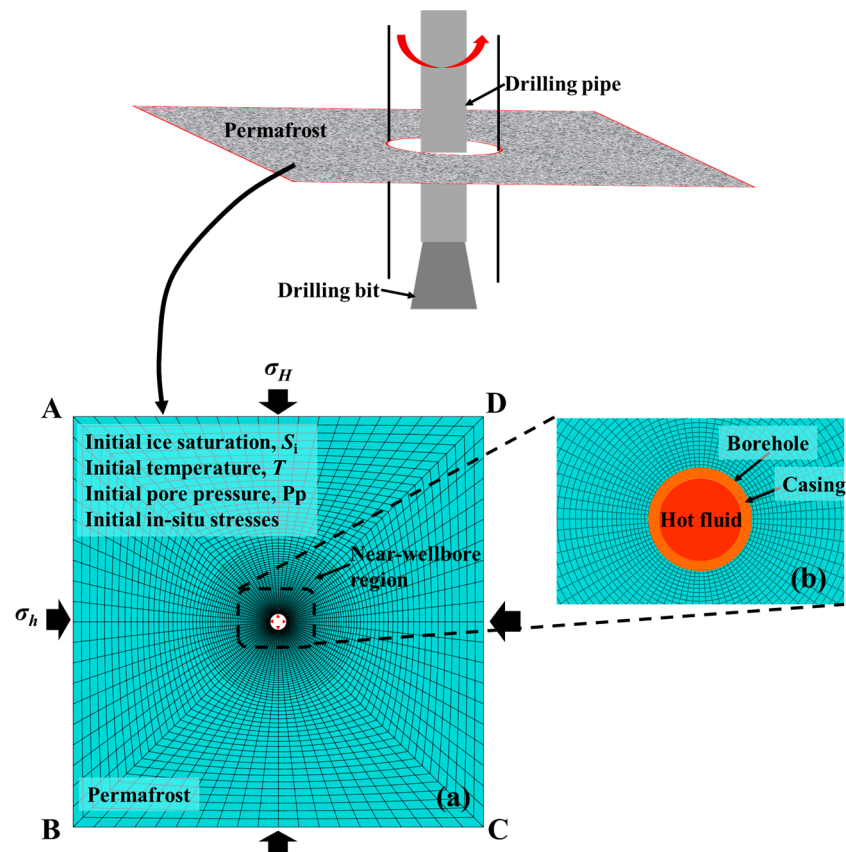
Figure 12. Model geometry used for investigating wellbore stability in permafrost. (**a**) Geometric model, (**b**) Mesh model.

Table 3. Basic data for simulation.

	Parameters	Unit	Value
Permafrost	Thermal conductivity	W/(m·°C)	2.5
	Density	kg/m^3	2600
	Porosity	%	20
	Specific heat capacity	J/(kg·°C)	850
	Depth	m	300
	Geothermal gradient	°C/100 m	3
	Temperature	°C	−10
	In-situ stresses	σH = 7.64 MPa, σh = 6.11 MPa, σV = 7.64 MPa	
	Ice saturation	%	50
	Pore pressure	MPa	3.0
Drilling fluid	Temperature	°C	25
Ordinary casing	Thermal conductivity	W/(m·°C)	45
	Specific heat capacity	J/(kg·°C)	460
	Density	kg/m^3	7800
vacuum-insulated casing	Thermal conductivity	Determine by Equation (8)	
Drilling operation	Total time	h	48

5.5. Ice Melting in the Near-Wellbore Region

The temperature disturbance of the permafrost surrounding the wellbore caused by the thermal fluid in the wellbore will inevitably result in the ice melting first. The more intense the heat transfer during the drilling operation, the wider the ice melting area will certainly be [10,42]. Therefore, by comparing the range of ice melting around the wellbore when ordinary casing and vacuum-insulated casing were used, the thermal insulation performance of vacuum-insulated casing can be indirectly revealed.

Figure 13 shows the evolution of the ice melting range in the permafrost around the wellbore during the drilling operation. From Figure 13a, it can be clearly seen that the melting range of ice around the wellbore is narrow when the vacuum-insulated casing was used during drilling and completion operations. In this case, only a negligible width of ice melting area appears around the wellbore. The quantification results (see Figure 13b) show that the width of this annular area is only 8.64 cm. Whereas, when the ordinary casing is used, the ice melts around the wellbore over a wide range. From Figure 13b, it can be seen that when the drilling operation has lasted for 48 h, the melting range of ice around the wellbore is as wide as 54 cm. For this case (ordinary casing), such a wide range of ice melting area is likely to pose a threat to the integrity of wellbore. By comparison, the use of vacuum-insulated casing can significantly weaken the melting of ice around the wellbore. Furthermore, it can be inferred from Figure 13 that as the drilling operation continues, the difference in the ice-melting range between the two cases will become more significant.
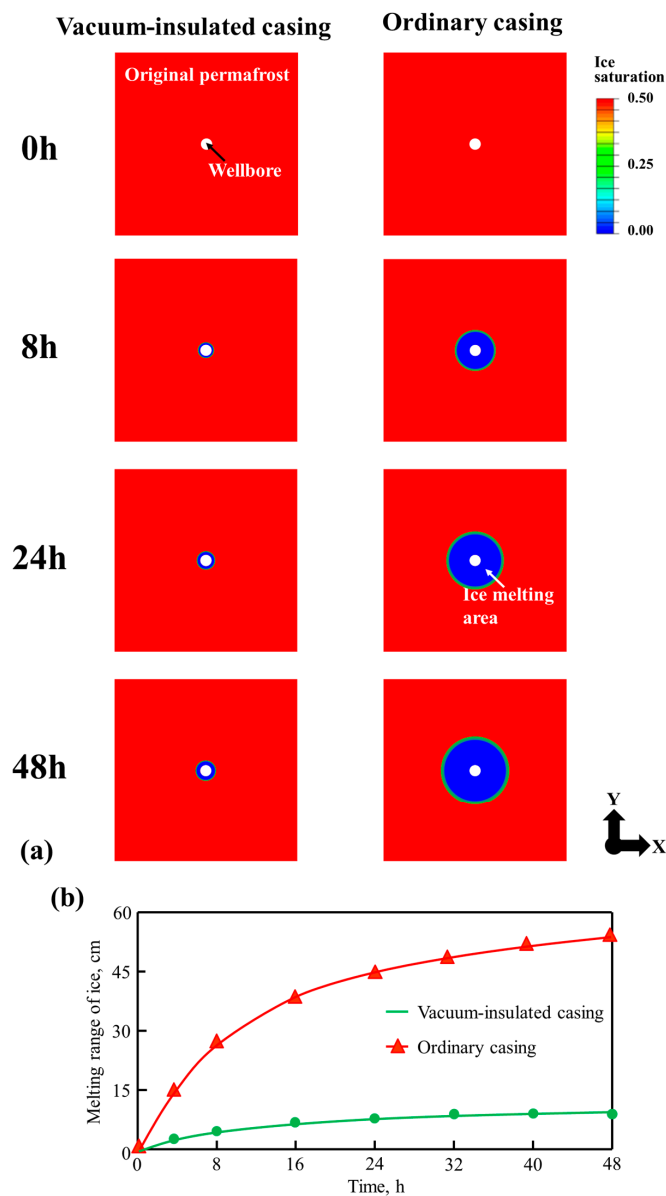

Figure 13. Ice melting in the permafrost around wellbore during the drilling operation. (**a**) Distribution of ice saturation, (**b**) evolution curves of ice-melting range.

The reason for the comparison results shown in Figure 13 can be attributed to the difference in the thermal insulation performance of the two casings. Figure 14 shows the

heat transfer throughout the drilling process when vacuum-insulated casings and ordinary casings are used, respectively. From Figure 14, it can be observed that the heat transferred during the investigation process is consistent with the evolution characteristics of the melting range of ice in Figure 13. Of course, this is applicable to both types of casing. The cumulative heat transferred during the entire simulation process when the ordinary casing was used is 424.24 KJ/m. However, only 64.69% of the heat is used for ice melting, while the rest is used to the increase in the sediment temperature. For the vacuum-insulated casing, the total heat transferred during the entire simulation process is 56.32 KJ/m, which is only 13.28% of that when the ordinary casing was used. Despite this, the proportion of heat used for ice melting in the near-wellbore region is not reduced compared to that when an ordinary casing is used. It remains at a high 76.84%. This indicates that for either type of casing, the majority of the heat transfer was used for the melting of ice in permafrost, with a proportion of over 60%. Only less than 40% of the heat transferred from the hot fluid inside the casing to the permafrost around the wellbore is used for the increase in sediment temperature. In this way, use of the vacuum-insulated casing to prevent uncontrolled heat transfer is an effective strategy to prevent the melting of ice around the wellbore while drilling in permafrost.
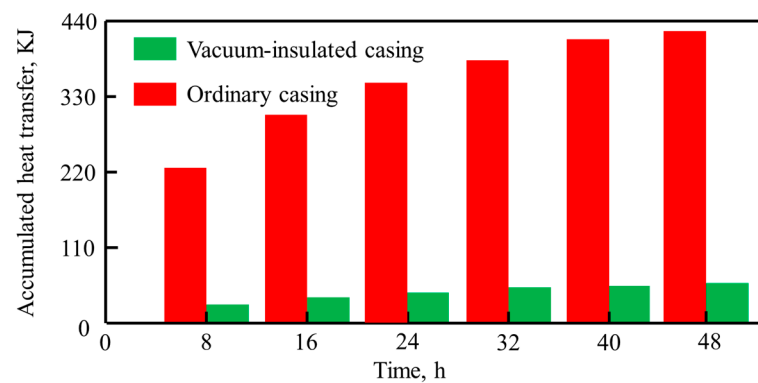

Figure 14. Heat transfer for two cases investigated in Figure 13.

5.6. Behaviorof Borehole Instability and Drilling Optimization

As mentioned above, as a type of cement, ice can enhance the strength of permafrost. On the contrary, the melting of ice in permafrost can lead to a weakening of its strength, which affects the stability of sediments. Then, the phase change of the ice around the wellbore during the drilling operation will inevitably affect the behavior of wellbores in permafrost. Borehole collapse is a common mode of wellbore instability in temperature-sensitive sediments such as permafrost and hydrate deposits [10,43]. In this section, the instability behavior of the wellbore when two types of casing were used was compared to highlight the superiority of the vacuum-insulated casing.

Figure 15 demonstrates the distribution of the final yield area around the wellbore when the vacuum-insulated casing and ordinary casing were used, respectively. From Figure 15, it can be clearly seen that the yield area in the near-wellbore region when the vacuum-insulated casing was used is much smaller than that when the ordinary casing was used. For the case when the vacuum-insulated casing was used, the yield point does not appear on the borehole in the direction of the minimum horizontal principal stress until the drilling operation continues for 8 h. Meanwhile, the yield area around the wellbore can be almost disregarded during a 48 h drilling operation (see Figure 15a). Moreover, the two yield areas symmetrically distributed around the wellbore are distributed independently throughout the simulation and do not connect with each. However, in the case of ordinary casing, the time when the yield point appears on the borehole has been advanced to 1.83 h after the start of the drilling operation (see Figure 15b). Furthermore, after the drilling operation lasted for 8 h, the two symmetrically distributed yield regions had been

integrated into one. During subsequent drilling operations, the yield area will expand in both the radial and circumferential directions.
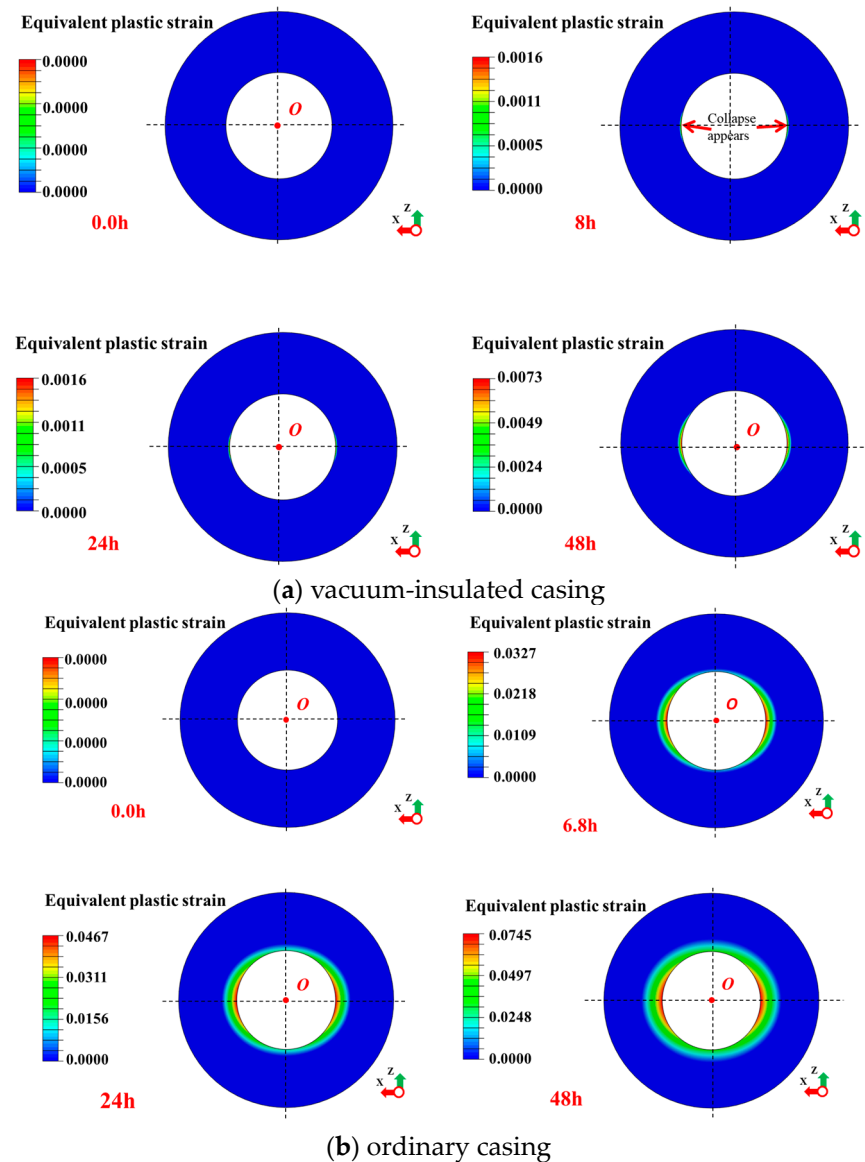

(**a**) vacuum-insulated casing

(**b**) ordinary casing

Figure 15. Distribution of the final yield region around wellbore for both cases.

To facilitate the quantification of wellbore instability and subsequent sand production, the yield area is defined using the following equation with the parameter δ [10,44]. It is obvious that a larger value of parameter δ indicates a higher possibility of wellbore instability and subsequent sand production.

$$\delta = \frac{A_{yield}}{A_{wellbore}} \times 100\% \tag{26}$$

where A_{yield} and $A_{wellbore}$ are the cross-section area of the yield region and wellbore in m^2.

Figure 16 shows the evolution curve of parameter δ for the two cases in Figure 14. It can be seen from Figure 16 that the parameter δ for the case of ordinary casing at any time of the drilling operation is much smaller than that for the vacuum-insulated casing. If the ordinary casing was used in the drilling operation, the final parameter δ is 52.1%. However, in the case of the vacuum-insulated casing, this value becomes 4.2%. It can be

concluded that the use of vacuum-insulated casing is beneficial in weakening the melting of ice around wellbore, as well as alleviating wellbore instability.
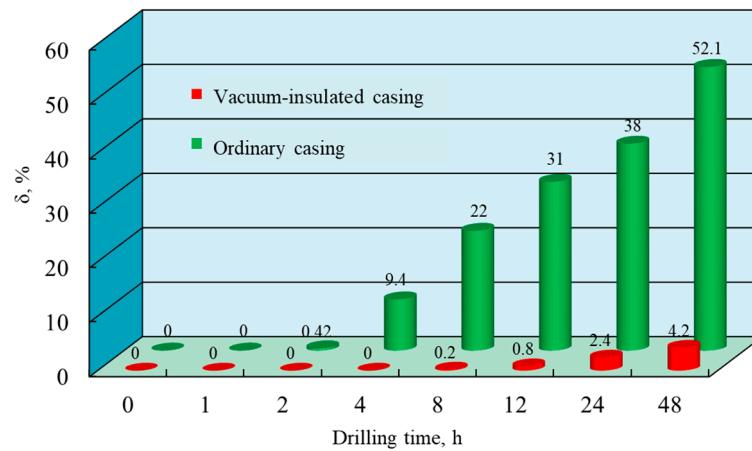

Figure 16. Evolution curve of parameter δ.

In fact, this does not mean that the ordinary casing is not suitable for drilling operations in permafrost. By increasing the ROP, the drilling operation cycle can be shortened, thereby reducing the disturbance of drilling operation on the stability of ice and the wellbore. However, the question is, how long should the drilling-operation cycle be designed to be? For drilling operations, moderate wellbore instability is accepted. Based on the simulation results, Table 4 presents the drilling optimization for both casings when acceptable δ is different. From Table 4, we can see that the acceptable drilling operation cycle for the vacuum-insulated casing is longer than that for the ordinary casing. For example, if $\delta = 5\%$ is acceptable, the drilling-operation cycle for the case of ordinary casings should be designed for less than 2.7 h. However, if the vacuum-insulated casing was used, the maximum drilling operation cycle was extended to 48 h. In this way, the difficulty of the drilling operation will be significantly reduced if the vacuum-insulated casing is used.

Table 4. Drilling optimization for both casings when the acceptable δ is different.

Casing Type	Maximum Drilling Operation Cycle, h			
	$\delta = 0$	$\delta = 5\%$	$\delta = 10\%$	$\delta = 15\%$
Ordinary casing	1.83	2.7	4.3	5.8
Vacuum-insulated casing	8.0	48.0	48.0	48.0

6. Conclusions and Future Work

In this study, the influence of various factors on the apparent thermal conductivity of the vacuum-insulated casing was experimentally explored. Based on the experimental results, the effectiveness or role of the vacuum-insulated casing in alleviating the melting of ice around the wellbore and the accompanying wellbore instability was numerically analyzed by comparison. The main conclusions made are as follows:

(1) The experimental system and method described in this study can be used for the measurement of the apparent thermal conductivity of the vacuum-insulated casings. The difference between the measured apparent thermal conductivity value and the true value of the ordinary casing with known thermal conductivity is less than 1.0 W/(m· °C).

(2) The insulation performance of the vacuum-insulated casing decreases with increasing fluid and ambient temperatures. The reason is that an increase in temperature activates the vibration of molecules inside the vacuum-insulation layer. Moreover, an increase in the vacuum degree fills the vacuum-insulation layer with more gas molecules, and

the thermal conductivity naturally increases accordingly. Interestingly, changes in these factors exhibit limited effects on the apparent thermal conductivity of vacuum-insulated casing. When the values of these factors exceed a certain threshold, their influence will be significantly weakened.

(3) The use of vacuum-insulated casing in drilling operations can effectively curb the heat transfer and prevent the uncontrolled melting of ice around the wellbore, as well as borehole instability. Compared to ordinary casing, the use of vacuum-insulated casing can decrease 86.72% of heat transferred in drilling operations and 84% of ice melting. Furthermore, most of the yield area (potential instability area) around the wellbore can also be avoided.

(4) Vacuum-insulated casing effectively alleviates the challenges of drilling operations in permafrost. For the same requirements for wellbore stability, the use of vacuum-insulated casing allows for longer drilling cycles and moderate ROPs. When the ordinary casing was used, the ROPs needed to be increased to shorten the drilling cycle and avoid the risk of uncontrollable wellbore instability.

In the future work, there are still many investigations that need to be conducted. Firstly, the impact of various factors on wellbore stability during drilling operations in permafrost needs to be further explored. Furthermore, the method for determining the safe mud temperature and weight window based on numerical analysis of wellbore stability also needs to be explored.

Author Contributions: Conceptualization, X.Z. and Y.S.; methodology, X.Z.; formal analysis, X.Z.; investigation, X.Z. and Y.C.; resources, X.Z.; writing—original draft preparation, X.Z. and Q.L.; writing—review and editing, X.Z. and Y.C.; visualization, X.Z.; supervision, Y.S. and Y.C.; project administration, X.Z. and Y.C.; funding acquisition, Y.C. All authors have read and agreed to the published version of the manuscript.

Data Availability Statement: Data are contained within the article.

Conflicts of Interest: The authors declare no conflict of interest.

References

1. Zhao, X.; Geng, Q.; Zhang, Z.; Qiu, Z.; Fang, Q.; Wang, Z.; Yan, C.; Ma, Y.; Li, Y. Phase change material microcapsules for smart temperature regulation of drilling fluids for gas hydrate reservoirs. *Energy* **2023**, *263*, 125715. [CrossRef]
2. Li, Q.; Cheng, Y.; Li, Q.; Ansari, U.; Liu, Y.; Yan, C.; Lei, C. Development and verification of the comprehensive model for physical properties of hydrate sediment. *Arab. J. Geosci.* **2018**, *11*, 325. [CrossRef]
3. Tang, X.; Zhang, B.; Höök, M.; Feng, L. Forecast of oil reserves and production in Daqing oilfield of China. *Energy* **2010**, *35*, 3097–3102. [CrossRef]
4. He, Y.; Qiao, Y.; Qin, J.; Tang, Y.; Wang, Y.; Chai, Z. A novel method to enhance oil recovery by inter-fracture injection and production through the same multi-fractured horizontal well. *J. Energ. Resour. Technol.* **2022**, *144*, 043005. [CrossRef]
5. Jin, Z.; Liang, X.; Bai, Z. Exploration breakthrough and its significance of Gulong lacustrine shale oil in the Songliao Basin, Northeastern China. *Energy Geosci.* **2022**, *3*, 120–125. [CrossRef]
6. Yuan, S.; Lei, Z.; Li, J.; Yao, Z.; Li, B.; Wang, R.; Liu, Y.; Wang, Q. Key theoretical and technical issues and countermeasures for effective development of Gulong shale oil, Daqing Oilfield, NE China. *Pet. Explor. Dev.* **2023**, *50*, 638–650. [CrossRef]
7. Wang, Q.; Li, S.; Li, R. China's dependency on foreign oil will exceed 80% by 2030: Developing a novel NMGM-ARIMA to forecast China's foreign oil dependence from two dimensions. *Energy* **2019**, *163*, 151–167. [CrossRef]
8. Zhu, J.; Chen, G.; Yin, Z.; Khan, F.; Meng, X. An integrated methodology for dynamic risk evaluation of deepwater blowouts. *J. Loss Prev. Process Ind.* **2022**, *74*, 104647. [CrossRef]
9. Li, Q.; Cheng, Y.; Li, Q.; Zhang, C.; Ansari, U.; Song, B. Establishment and evaluation of strength criterion for clayey silt hydrate-bearing sediments. *Energy Sources Part A Recovery Util. Environ. Eff.* **2018**, *40*, 742–750. [CrossRef]

10. Li, Q.; Liu, J.; Wang, S.; Guo, Y.; Han, X.; Li, Q.; Cheng, Y.; Dong, Z.; Li, X.; Zhang, X. Numerical insights into factors affecting collapse behavior of horizontal wellbore in clayey silt hydrate-bearing sediments and the accompanying control strategy. *Ocean Eng.* **2024**, *297*, 117029. [CrossRef]
11. Liu, H.; Liu, H.; Zhang, Q.; Fan, M.; Yin, B.; Wang, X.; Sun, X.; Wang, Z. Effect of liquid viscosity on the gas-liquid two phase countercurrent flow in the wellbore of bullheading killing. *Geoenergy Sci. Eng.* **2023**, *221*, 111274. [CrossRef]
12. Zhang, Z.; Sun, B.; Wang, Z.; Pan, S.; Lou, W.; Sun, D. Early monitoring method of downhole accident driven by physics based model and data driven methods coupling. *Geoenergy Sci. Eng.* **2023**, *221*, 111296. [CrossRef]
13. Li, Q.; Wang, Y.; Wang, F.; Li, Q.; Kobina, F.; Bai, H.; Yuan, L. Effect of a modified silicone as a thickener on rheology of liquid CO_2 and its fracturing capacity. *Polymers* **2019**, *11*, 540. [CrossRef] [PubMed]
14. Chen, X.; He, M.; Xu, M.; Wang, S.; Dai, B. Early gas kick detection-inversion-control integrated system: The significance of applications of managed pressure drilling: A review. *Geoenergy Sci. Eng.* **2023**, *229*, 212134. [CrossRef]
15. Yang, H.; Li, J.; Jiang, J.; Zhang, H.; Guo, B.; Zhang, G.; Chen, W. A dynamic managed pressure well-control method for rapid treatment of gas kick in deepwater managed pressure drilling. *Pet. Sci.* **2022**, *19*, 2297–2313. [CrossRef]
16. Gu, Q.; Fallah, A.; Feng, T.; Bakshi, S.; Chen, D.; Ashok, P.; Moore, D.; Oort, E. A novel dilution control strategy for gas kick handling and riser gas unloading mitigation in deepwater drilling. *J. Pet. Sci. Eng.* **2021**, *196*, 107973. [CrossRef]
17. Noynaert, S.; Jerome, J. Modeling ultra-deepwater blowouts and dynamic kills and the resulting blowout control best practices recommendations. In Proceedings of the SPE/IADC Drilling Conference and Exhibition, SPE, Amsterdam, The Netherlands, 23–25 February 2005; p. SPE-92626-MS.
18. Yuan, Z.; Hashemian, Y.; Morrell, D. Ultra-deepwater blowout well control analysis under worst case blowout scenario. *J. Nat. Gas Sci. Eng.* **2015**, *27 Pt 1*, 122–129. [CrossRef]
19. Ren, W.; Fan, H.; Deng, S.; Cui, C.; Peng, Q.; Liu, X.; Dou, X. Displacement Calculation of Dynamic Killing Drilling. In Proceedings of the SPE Nigeria Annual International Conference and Exhibition, Lagos, Nigeria, 4–6 August 2015; p. SPE-178362-MS.
20. Lu, J.; Zhang, M.; Zhang, X.; Pei, W.; Bi, J. Experimental study on the freezing–thawing deformation of a silty clay. *Cold Reg. Sci. Technol.* **2018**, *151*, 19–27. [CrossRef]
21. Wen, Y.; Liu, L.; Huang, Y.; Liu, H.; Sui, M. Cause Analysis and Preventive Measures for Sand Production in Gas Wells of Sulige Gas Field. *ACS Omega* **2023**, *8*, 30590–30597. [CrossRef]
22. Wei, Y.; Xiong, Y.; Liu, Z.; Lu, J. Thermal diffusion characteristics in permafrost during the exploitation of gas hydrate. *Geofluids* **2021**, *2021*, 6620288. [CrossRef]
23. Ben Mahmud, H.; Leong, V.H.; Lestariono, Y. Sand production: A smart control framework for risk mitigation. *Petroleum* **2020**, *6*, 1–13. [CrossRef]
24. Garolera, D.; Carol, I.; Papanastasiou, P. Micromechanical analysis of sand production. *Int. J. Numer. Anal. Methods Geomech.* **2019**, *43*, 1207–1229. [CrossRef]
25. Wang, X.; Wang, Z.; Deng, X.; Sun, B.; Zhao, Y.; Fu, W. Coupled thermal model of wellbore and permafrost in Arctic regions. *Appl. Therm. Eng.* **2017**, *123*, 1291–1299. [CrossRef]
26. Kutasov, I.M.; Eppelbaum, L.V. Time of refreezing of surrounding the wellbore thawed formations. *Int. J. Therm. Sci.* **2017**, *122*, 133–140. [CrossRef]
27. Zhou, X.; Su, Y.; Cheng, Y.; Li, Q. Preliminary Insight into Ice Melting, Surface Subsidence, and Wellhead Instability during Oil and Gas Extraction in Permafrost Region. *Energies* **2024**, *17*, 1292. [CrossRef]
28. Wang, K. Simulation and Analysis of Wellbore Stability in Permafrost Formation with FLAC. Ph.D. Dissertation, University of Alaska Fairbanks, Fairbanks, AK, USA, 2015.
29. Xie, J.; Matthews, C.M. Methodology to assess thaw subsidence impacts on the design and integrity of oil and gas wells in Arctic regions. In Proceedings of the SPE Arctic and Extreme Environments Technical Conference and Exhibition, Moscow, Russia, 18 October 2011; p. SPE-149740-MS.
30. Atlasov, R.; Nikolaeva, M.; Karamzin, V. Development of drilling and casing technologies for permafrost areas. *IOP Conf. Ser. Earth Environ. Sci.* **2019**, *272*, 022078. [CrossRef]
31. Yanhu, M.; Guoyu, L.; Wei, M.; Zhengmin, S.; Zhiwei, Z.; Wang, F. Rapid permafrost thaw induced by heat loss from a buried warm-oil pipeline and a new mitigation measure combining seasonal air-cooled embankment and pipe insulation. *Energy* **2020**, *203*, 117919. [CrossRef]
32. Romanovsky, V.; Smith, S.; Christiansen, H. Permafrost thermal state in the polar Northern Hemisphere during the international polar year 2007-2009: A synthesis. *Permafr. Periglac* **2010**, *21*, 106–116. [CrossRef]
33. Yamamoto, Y.; Springman, S. Axial compression stress path tests on artificial frozen soil samples in a triaxial device at temperatures just below 0 °C. *Can Geotech J.* **2014**, *51*, 1178–1195. [CrossRef]
34. Misyurkeeva, N.; Buddo, I.; Kraev, G.; Smirnov, A.; Nezhdanov, A.; Shelokhov, I.; Belonosov, A. Periglacial Landforms and Fluid Dynamics in the Permafrost Domain: A Case from the Taz Peninsula, West Siberia. *Energies* **2022**, *15*, 2794. [CrossRef]
35. Wang, J.; Zhang, F.; Yang, Z.; Yang, P. Experimental investigation on the mechanical properties of thawed deep permafrost from the Kuparuk River Delta of the North Slope of Alaska. *Cold Reg. Sci. Technol.* **2022**, *195*, 103482. [CrossRef]
36. Deng, X.; Pan, S.; Wang, Z.; Ke, K.; Zhang, J. Application of the Darcy-Stefan model to investigate the thawing subsidence around the wellbore in the permafrost region. *Appl. Therm. Eng.* **2019**, *156*, 392–401. [CrossRef]

37. Yang, Z.; Still, B.; Ge, X. Mechanical properties of seasonally frozen and permafrost soils at high strain rate. *Cold Reg. Sci. Technol.* **2015**, *113*, 12–19. [CrossRef]

38. Bilodeau, J.; Verreault, J.; Doré, G. Assessment of the physical and mechanical properties of permafrost in Nunavik, Quebec, Canada. In Proceedings of the 18th International Conference on Cold Regions Engineering and 8th Canadian Permafrost Conference, Quebec City, QC, USA, 19–21 August 2019; pp. 17–25.

39. Arenson, L.; Johansen, M.; Springman, S. Effects of volumetric ice content and strain rate on shear strength under triaxial conditions for frozen soil samples. *Permafr. Periglac.* **2004**, *15*, 261–271. [CrossRef]

40. Rostami, A. Stability Analysis of Frozen Soil Slopes Considering Strain Localization. Ph.D. Dissertation, Concordia University, Montreal, QC, Canada, 2022.

41. Bai, R.; Lai, Y.; Pei, W.; Zhang, M. Investigation on frost heave of saturated–unsaturated soils. *Acta Geotech.* **2020**, *15*, 3295–3306. [CrossRef]

42. Nassr, A.; Esmaeili-Falak, M.; Katebi, H.; Javadi, A. A new approach to modeling the behavior of frozen soils. *Eng. Geol.* **2018**, *246*, 82–90. [CrossRef]

43. Zhang, Y. Thermal-Hydro-Mechanical Model for Freezing and Thawing of Soils. Ph.D. Dissertation, University of Michigan, Ann Arbor, MI, USA, 2014.

44. Yao, X.; Qi, J.; Wu, W. Three dimensional analysis of large strain thaw consolidation in permafrost. *Acta Geotech.* **2012**, *7*, 193–202. [CrossRef]